Title

Overview of HL-2A recent experiments

Journal

Nuclear Fusion, 59(11)

ISSN

0029-5515

Authors

Xu, M

Duan, XR

Liu, Yi

et al.

Publication Date

2019-11-01

DOI

10.1088/1741-4326/ab1d84

Peer reviewed

Author's accepted manuscript
Published as: *Nucl. Fusion* 59, 112017, 2019
https://doi.org/10.1088/1741-4326/ab1d84

OVERVIEW OF HL-2A RECENT EXPERIMENTS

M. XU[1], X.R. DUAN[1], YI LIU[1], X.M. SONG[1], D.Q. LIU[1], Y.Q. WANG[1], B. LU[1], Q.W. YANG[1], G.Y. ZHENG[1], X.T. DING[1], J.Q. DONG[1], G.Z. HAO[1], W.L. ZHONG[1], Z.B. SHI[1], L.W. YAN[1], X.L. ZOU[2], Y.Q. LIU[3,1], W. CHEN[1], G.L. XIAO[1,4], Y.P. ZHANG[1], M. JIANG[1], Y.M. HOU[1,5], J. CHENG[1], A.S. LIANG[1], X.Y. BAI[1], J.Y. CAO[1], Z. CAO[1], H.T. CHEN[1], C.H. CUI[1], Z.Y. CUI[1], L. DELPECH[2], P.H. DIAMOND[6], A. EKEDAHL[2], B.B. FENG[1], G. GIRUZZI[2], S.B. GONG[1,5], H.M. HE[1], T. HOANG[2], M. HUANG[1], Y. HUANG[1], K. IDA[7], S. INAGAKI[8], M. ISOBE[7], K. ITOH[9,7], S.-I. ITOH[10,8], X.Q. JI[1], R. KE[1], M. KOBAYASHI[7], G.J. LEI[1], B. LI[1], G.S. LI[1], H.J. LI[1], J.Q. LI[1], Q. LI[1], QING LI[1], X.D. LI[1], Y.G. LI[1], YONGGE LI[1], W.C. MAO[1], D. MAZON[2], G.R. MCKEE[11], S. MORITA[7], L. NIE[1], J.F. PENG[1], Y. PEYSSON[2], J. RAO[1], Y. REN[12], G.R. TYNAN[13], H.X. WANG[1,4], Q.M. WANG[1], H.L. WEI[1], F. XIA[1], X.P. XIAO[1], W.M. XUAN[1], Z. YAN[11], K. YAO[1], L.M. YU[1], Y. YU[5], D.L. YU[1], B.D. YUAN[1,5], B.S. YUAN[1], J.H. ZHANG[1], Y. ZHOU[1], YONG LIU[1] AND HL-2A TEAM

[1]Southwestern Institute of Physics, P. O. Box 432, Chengdu 610041, China
[2]CEA, IRFM, F-13108 Saint-Paul-lez-Durance, France
[3]General Atomics, San Diego, California, USA
[4]Tsinghua University, Beijing , China
[5]University of Science and Technology of China, Hefei, China
[6]CASS and Department of Physics, UCSD, La Jolla, CA 92093, USA
[7]National Institute for Fusion Science, 322-6 Oroshi-cho, Toki-shi 509-5292, Japan
[8]Research Institute for Applied mechanics, Kyushu University, Kasuga, Kasugakeon 6-1, 816-8580, Japan
[9] Institute of Science and Technology Research, Chubu University, 487-8501, Japan
[10]Research Center for Plasma Turbulence, Kyushu University, 816-8580 Japan
[11]University of Wisconsin-Madison, Madison, Wisconsin, USA
[12]Princeton Plasma Physics Laboraroty, Princeton, NJ 08540, USA
[13]CMTFO, University of California San Diego, La Jolla, CA 92093, USA

E-mail: minxu@swip.ac.cn

Abstract. The mission of HL-2A is to explore the key physical topics relevant to

ITER and to the advanced tokamak operation (e.g. the operation of future HL-2M), such as the access of H-mode, energetic particle physics, edge-localized mode (ELM) mitigation/suppression and disruption mitigation. Since the 2016 Fusion Energy Conference, the HL-2A team has focused on the investigations on the following areas: (i) pedestal dynamics and L-H transition, (ii) techniques of ELM control, (iii) the turbulence and transport, (iv) energetic particle physics. The HL-2A results demonstrated that the increase of mean $E \times B$ shear flow plays a key role in triggering L-I and I-H transitions. While the change of $E \times B$ flow is mainly induced by the ion pressure gradient. Both mitigation and suppression of ELMs were realized by laser blow-off (LBO) seeded impurity (Al, Fe, W). The 30% Ne mixture supersonic molecular beam injection (SMBI) seeding also robustly induced ELM mitigation. The ELMs were mitigated by low-hybrid current drive (LHCD). The stabilization of m/n=1/1 ion fishbone activities by electron cyclotron resonance heating (ECRH) was found on the HL-2A. A new m/n=2/1 ion fishbone activity was observed recently, and the modelling indicated that passing fast ions dominantly contribute to the driving of 2/1 fishbone. The non-linear coupling between toroidal Alfven eigenmode (TAE) and tearing mode (TM) leads to the generation of a high frequency mode with the toroidal mode number n=0. The turbulence is modulated by tearing mode when the island width exceeds a threshold and the modulation is localized merely in the inner area of the islands. Meanwhile, turbulence radially spreading takes place across the island region.

1. Introduction

The mission of HL-2A is to explore the key physical topics relevant to ITER and to the advanced operation of tokamak(e.g. the operation of future HL-2M), such as the access of H-mode, energetic particle physics, edge localized mode (ELM) mitigation/suppression and disruption mitigation. The HL-2A is a conventional tokamak with the major radius $R = 1.65$ m and the minor radius $a \simeq 0.4$ m. The toroidal magnetic field, plasma current, and central line-averaged density are $B_T = 1.3 - 2.7$ T, $I_p = 150 - 430$ kA, and $n_{e0} = (1 - 6) \times 10^{19}$ m^{-3}, respectively. The electron and ion temperatures are up to $T_e = 5$ keV and $T_i = 2.8$ keV, respectively.

The auxiliary heating power has been updated since 2016. The second neutral beam injection (NBI) line was developed. Now the highest parameter for single beam source exceeds 15 A $\times$ 40 kV, the injection power of this source exceeds 0.4 MW, and the total NBI injection power exceeds 1.2 MW in 2018 campaign. The low-hybrid wave (LHW)/current drive (LHCD) power coupling was optimized using the Passive-Active Multi-junction (PAM) antenna, by which the coupled power reached 1.4 MW in H-mode plasma in 2018. As the benefits of the updated auxiliary heating power, the achieved parameters of the HL-2A were improved. The achieved normalized beta (β_N) exceeds 2.5. The poloidal beta (β_p) reaches 2.0. Good confinement of plasma was obtained with $H_{98} \sim 1.2$. The fully non-inductive discharge was realized for the first time on the HL-2A device in 2018 campaign (Fig.1). These updates and the improvement of the

operation regime significantly enhance the capability for the studies on the advanced plasma physics on the HL-2A.

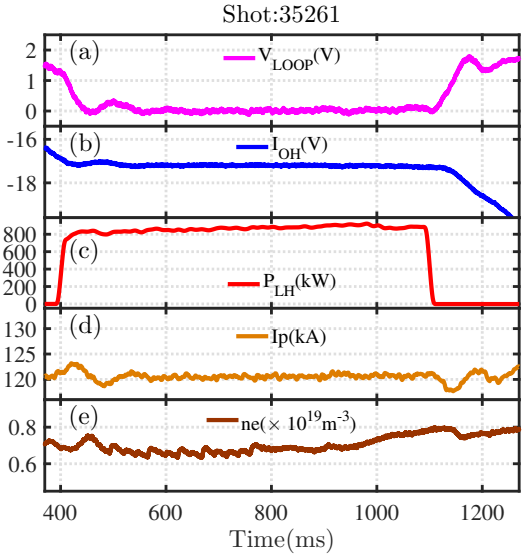

Figure 1: Time evolution of main parameters for the fully non-inductive discharge.

Since the 2016 Fusion Energy Conference, the HL-2A team has focused on the investigations on the following areas: (i) pedestal dynamics and L-H transition, (ii) techniques and physics of ELM control, (iii) the turbulence and transport, (iv) energetic particle physics. The highlights of the experimental results are summarized in this paper, while the detailed descriptions can be found in the corresponding references.

2. PEDESTAL DYNAMICS AND L-H TRANSITION

In H-mode plasma of magnetically confined devices, the pedestal plays a key role in governing the performance of the core plasma by providing a boundary condition for the stiff core transport. To improve the plasma stability and confinement, it is important to study the pedestal dynamics and understand the underlying physics. This section reports the pedestal dynamics prior to ELM burst and the role of electric field shear in the L-I and L-H transitions.

2.1. Pedestal dynamics

In pedestal region, the increases of density and its gradient were observed prior to each ELM onset in a series. An inward particle flux induced by quasi-coherent mode (QCM) ($f = 30 - 70$ kHz) was found to be responsible for such changes. The mode localizes in the pedestal, leads to the increase of density gradient, and has strong nonlinear interaction with the turbulence.

Phase 1 in Fig.2 is characterized by the evolution of the edge pedestal without distinct coherent fluctuation. Phase 2 is denoted by the shading area with a duration

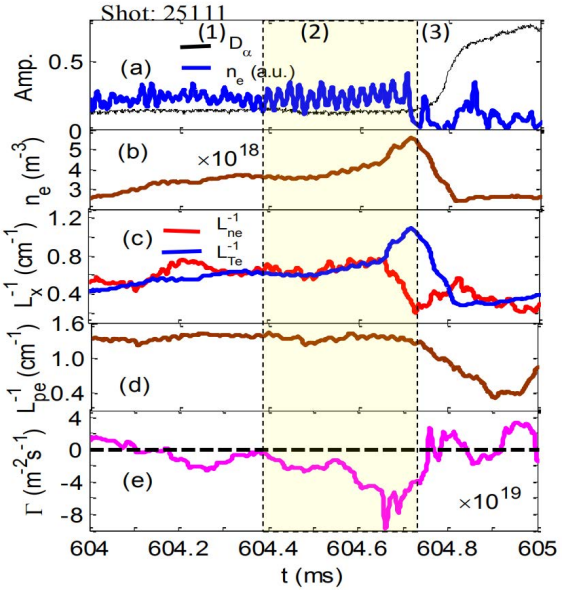

Figure 2: Temporal evolutions of D_α and the density fluctuation (a), the pedestal density (b), the inverses gradient scale lengths of the density and electron temperature (c), electron pressure (d), and the particle flux induced by the QCM (e).

time about 300 ms. In this phase the coherent fluctuation gradually grows, saturates and starts to decay, and the mode is radially localized with frequency $\sim$ 30-70 kHz. The electron density, measured by the Langmuir probe, keeps increasing until the end of this phase (Fig.2(b)), similar to the observation by microwave diagnostics. The L_{ne}^{-1} decreases abruptly at the end of this phase, while L_{Te}^{-1} increases obviously (Fig.2(c)), keeping the L_{pe}^{-1} changing moderately (d). Here, L_{ne}^{-1}, L_{Te}^{-1}, and L_{pe}^{-1} are the inverses gradient scale lengths of the electron temperature, density and the pressure, respectively. The QCM induced inward particle flux also increases firstly and then decreases (Fig.2(e)). The abrupt variations of electron temperature, density and particle flux indicate a dynamic transition of the plasma prior to the ELM onset. The most striking point here is that the inward particle is synchronized with the appearance of coherent mode, which can induce the particle transport channel coupling with the local density. In the following phase 3, the D_α emission increases dramatically. Meanwhile, n_e, L_{ne}^{-1}, and L_{pe}^{-1} decrease rapidly, and the amplitude of the QCM also damps. This is a phase of recovery, which smoothly connects to phase 1.

Experimental measurements indicates that (1) QCM is localized in the pedestal region with 2 $\sim$ 3 cm width; (2) QCM is an electromagnetic instability with the poloidal mode number being $m = 20 \sim 24$; (3) the mode structure is changed just before the onset of ELMs. Generation of QCM may be related to the nonlinear coupling of small scale turbulences. More detailed experimental and theoretical investigations are needed to make a final conclusion on the instability that affects the pedestal dynamics [1]. Quasi-coherent fluctuations was also observed on the C-Mod device [2].

2.2. L-H transition

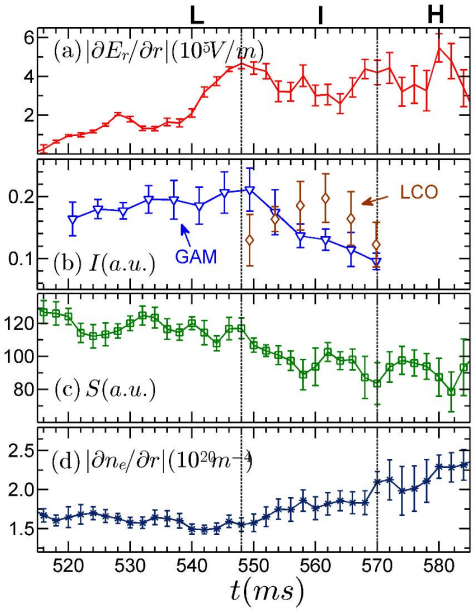

Figure 3: Time evolution of key parameters in the pedestal region (a) pedestal Er gradient, (b) GAM and LCO intensity, (c) turbulence intensity, (d) pedestal density gradient. Reproduced with the permission from [3]

In the pedestal region, the dynamics of the plasma flows, turbulence and pedestal formation across the L-I-H transitions was studied by using Doppler reflectometry [3]. Figure 3 shows the dynamics of shear flow and turbulence in the pedestal region. It indicates that the gradient of electric field $|\partial E_r/\partial r|$ suddenly increases in the L-mode and reaches a maximum value before the plasma transits into the I-phase. Meanwhile, the turbulence intensity (Fig. 3(c)) decreases slightly. After the L-I transition [4], the intensity of GAM starts to decrease but the intensity of limit cycle oscillation (LCO) increases immediately (Fig. 3(b)); while the turbulence intensity drops, suggesting that the LCO oscillatory flow regulates the turbulence, leading to the increase of density gradient $|\partial n_e/\partial r|$ (Fig. 3(d)). The intensity of LCO tends to decrease just prior to the I-H transition. It is worthy to note that the edge $|\partial E_r/\partial r|$ increases abruptly during the decreasing phase of these two oscillatory flows, and at the same time, the pedestal turbulence intensity undergoes a significant decrease. The drop of the LCO intensity may be induced by the increase of the mean $E \times B$ shear flow, which reduces the turbulence, leading to the decrease of LCO intensity. Simultaneously, the $|\partial n_e/\partial r|$ increases abruptly just before the I-H transition. All these observations suggest that mean $E \times B$ shear flow is responsible for both L-I and I-H transitions.

However, since the time resolution of the Doppler reflectometer for calculating the Doppler shift is about 1 ms, it cannot be excluded that very short pulse of turbulence driven shear flow (< 0.1 ms) can trigger L-H transitions as shown in [5]. Now the key question is what is the physical mechanism for the increase of mean $E \times B$ shear flow

just before the two transitions. The results show that the abrupt increase of $|\partial E_r/\partial r|$ observed prior to the L-I and I-H transitions is caused by the ion pressure component $|\partial E_r^{\nabla p_i}/\partial r|$, while the changes due to $|\partial E_r^{v_\theta}/\partial r|$ and $|\partial E_r^{v_\phi}/\partial r|$ are negligible [3]. Results on the ASDEX Upgrade also indicated that, in the pedestal region, E_r is mainly determined by the ion pressure gradient, when the toroidal flow is negligibly small [6].

Here, $E_r^{\nabla P_i}$, $E_r^{v_\phi}$ and $E_r^{v_\theta}$ denote the ion diamagnetic, toroidal velocity and poloidal velocity components of E_r, respectively. Whist in $\bigtriangledown p_i$ component, the contribution from ion temperature gradient is dominant over that from density gradient [3].

3. STUDIES ON THE ELM CONTROL

Based on the advantages of the H-mode, it has been chosen over the other improved confinement modes as the primary operating scenario for ITER. However, the strong gradient of plasma edge pressure can trigger repetitive edge-localized modes (ELMs) which usually produce high transient heat loads on plasma facing components (PFCs). Over many years, intensive efforts have been dedicated to finding an optimal and robust technique for heat load and ELM control. Especially, it is crucial to develop effective techniques to control ELM, in order to protect PFCs in burning plasma devices. This section presents the ELM control techniques applied on the HL-2A device.

3.1. ELM mitigation by LHCD

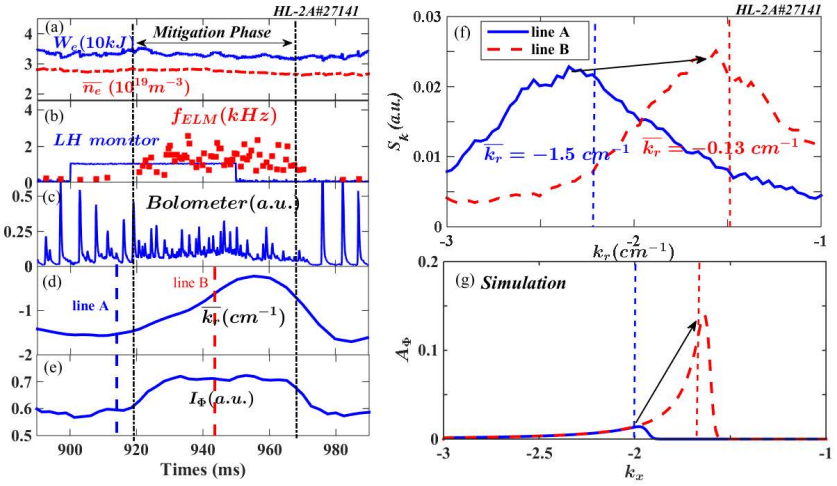

Figure 4: Analysis of ELM mitigation experiment with LHCD on HL-2A. (a) Plasma density (red dashed) and internal stored energy (blue solid); (b) the LHCD monitor signal (blue solid) and the ELM frequency (red solid square); (c) the bolometer signal; (d) the averaged radial wavenumber $\overline{k_r}$ of density fluctuation; (e) the pedestal turbulence intensity; (f) the radial wavenumber spectra before (blue solid) and during (red dashed) the ELM mitigation.(g) The simulation results of the turbulence spectral shift mode. spectra before (blue solid) and during (red dashed) the ELM mitigation.

On the HL2A, it is observed that ELMs are mitigated by LHCD, accompanied with significant reduction of divertor heat load peak [7]. The ELM mitigation phase is characterized by the increase of ELM frequency and the decrease of ELM amplitude. The averaged radial wavenumber $\overline{k_r}$ of density fluctuation shifts from a large negative value (about -1.5 cm $^{-1}$) to zero during mitigation phase (Fig.4(d)). The negative value of $\overline{k_r}$ means that the turbulence radially propagates inward. The spectral shift process is also observed (Fig.4(f)). Meanwhile, the turbulence intensity is enhanced during mitigation phase (Fig.4(e)). Thus, it suggests that the spectral shift process leads to the pedestal turbulence enhancement, which is responsible for the ELM mitigation. Here, the mechanism of ELM mitigation by LHCD is different with that observed on the EAST, which suggests that the magnetic topology changes induced by lower hybrid wave plays a key role in ELM mitigation [8].

Figure 4(b) shows that ELMs are still suppressed after the LHCD pulse is switched off. Actually, as reported in [7], LHCD is not a direct cause of ELM mitigation, but the turbulence enhancement is. LHCD modified the diamagnetic term of $E \times B$ velocity shear, which enhances the turbulence intensity by inducing a radial wavenumber spectral shift of turbulence. The turbulence enhancement is responsible for ELM mitigation possibly due to a nonlinear interaction process. Hence, ELMs remains mitigation when the pedestal turbulence is still enhancing even after the LHCD pulse is switched off.

In order to understand the mechanism of the turbulence enhancement during ELM mitigation, a turbulent heat transport model, based on the regulation of the turbulence amplitude by its radial wavenumber spectral shift caused by external velocity shear, was developed [9]. This external velocity shear can be produced by SMBI, impurity injection or LHCD. In this model, the external source induced velocity shear rate leads to the turbulence wavenumber spectrum shifting to zero direction (i.e. the normalized spectral averaged radial wavenumber ($\overline{k_x}$) approaches to zero). This shift reduces the dissipation term($\sim k_x^2$) and induces the increase the turbulence amplitude (A_Φ). Fig.4(g) displays the detailed spectral shift process with the increase of turbulence amplitude. The blue solid line represents the radial wavenumber spectrum at an earlier time of the shift process with lower turbulence amplitude. This simulation result indicates that the turbulence intensity is regulated by the radial wavenumber spectral shift, which agrees with the experimental results.

Based on the radial force balance equation, the external source input influences $E \times B$ shear by three terms: the spatial differential of the ion diamagnetic term, of the toroidal rotation term and of the poloidal rotation term. A sudden reduction of $E \times B$ velocity shear is observed after the application of LHCD on the HL-2A. This reduction is mainly induced by the spatial differential of the ion diamagnetic term [10].

3.2. ELM mitigation/suppression by impurity injection

The study on the effect of impurities on plasma confinement and pedestal instabilities, including ELMs and turbulence has been recently emphasized [11, 12, 13, 14]. Beneficial

effect of the pedestal deposited impurity injected by laser blow-off (LBO) on ELM mitigation/suppression was demonstrated in a controlled manner on the HL-2A. Here, LBO is used to inject three kinds of metal impurities (Al, Fe, W).

Both mitigation and suppression of ELMs were realized by LBO-seeded impurity. It was found that the occurrence of the ELM mitigation and ELM suppression sensitively depends on the LBO laser spot diameter. Measurements shown that the LBO-seeded impurity particles are mainly deposited in the pedestal region. In the ELM mitigation phase, the pedestal density fluctuation is significantly increased, indicating that the ELM mitigation may be achieved by the enhancement of the pedestal transport. More interestingly, the transition from ELM mitigation to ELM suppression was triggered when the number of the LBO-seeded impurity exceeds a threshold value [14].

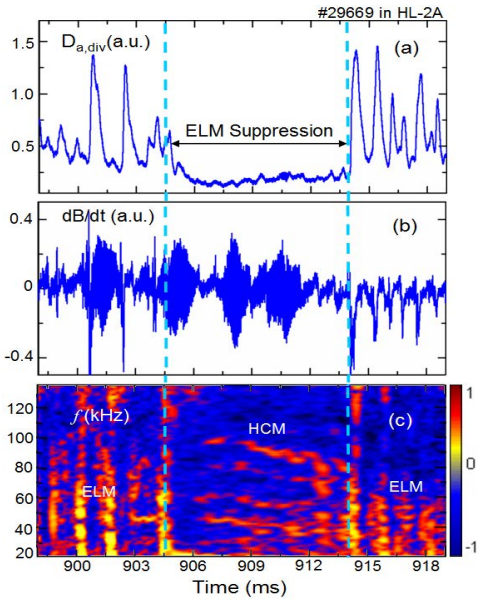

Figure 5: Observation of the harmonic coherent mode (HCM) during the ELM suppression phase. (a) Divertor D_α signal, (b) mirnov signal, and (c) time-frequency spectrum of the Mirnov signal. Here, LBO system was triggered at 900 ms for W impurity injection. Reproduced with the permission from [14]

In the ELM suppression phase, a harmonic coherent mode (HCM) is excited by the LBO-seeded impurity (Fig.5). The frequency range of HCM is from 10 to 100 kHz. However, the pedestal turbulence measured by the Doppler reflectometry is almost suppressed in the ELM suppression phase, which is different from the ELM mitigation phase. Furthermore, it was found that the strong interaction exists between different harmonics of HCM and background turbulence, and energy is transferred from the background turbulence to HCM. It suggests that HCM suppresses the pedestal turbulence, reduces the particle transport, and raises the plasma density. These suggest that HCM could extend the Peeling-Ballooning instability limit for ELM triggering, as predicted by theory [15]. As shown by the present experiments, HCM can not only be spontaneously excited in H-mode plasmas, but also externally excited by impurity

seeding. In the future, we will pursue the mechanism of the HCM excitation and of the transition from ELM mitigation to suppressing as increasing the amount of the injected impurity.

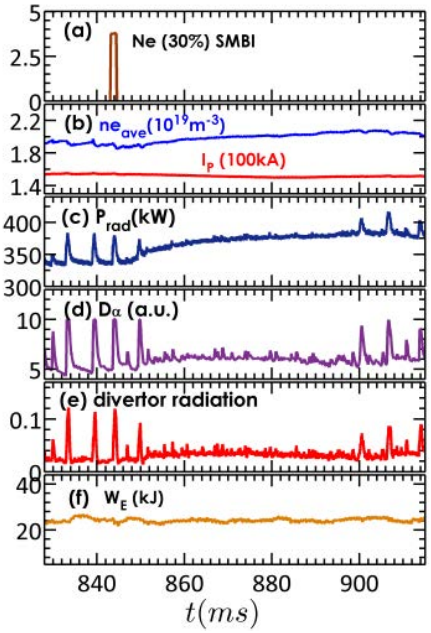

Figure 6: Time traces of main parameters for the impurity seeding experiment by using 30% Ne mixture SMBI on the HL-2A.

Another source injection technique, supersonic molecular beam injection (SMBI), is an effective method to control ELMs [16, 17, 18]. Besides pure impurity gas (Ne, Ar, etc), one species of impurity gas is mixed with main ion fuelling gas D_2 by different ratio during SMBI on the HL-2A. The first experiment on heat load and ELM control with impurity mixture SMBI seeding was carried out in H-mode plasmas in 2017. The impurity gases with different Ne ratios (10%, 30% and 100%) were seeded into the ELMy H-mode plasmas. It was observed that the ELM behavior varied with the impurity ratio of the mixture SMBI. For 10% Ne mixture SMBI, ELMs can be mitigated and this mitigation effect is similar to that of the main ion fuelling D_2. For 30% Ne mixture SMBI seeding, the ELMs are replaced by high frequency bursts (HFBs) with smaller amplitude as seen from the D_α in Fig.6(d) and divertor radiation signals in Fig.6(e).

The SMBI gradually increases the plasma density by $\sim 10\%$ in the ELMy H-mode (Fig. 6(b)). As expected, the total radiation power (Fig. 6(c)) increases after the SMBI. The evolution of the inner stored energy (Fig. 6(f)) shows that the global plasma confinement keeps almost constant. The time delay cross-correlation function was used to evaluate the correlation level between the divertor D_α signal and the electron densities during the occurrence of the HFBs. It indicates that the pedestal electron density is modulated by HFBs which originate from the pedestal region and propagate outwardly. HFBs enhance the pedestal particle transport and reduce the pedestal density gradient.

In the present mixture SMBI seeding experiments, no impurity core accumulation was observed, and the plasma confinement was unaffected. The divertor heat flux and radiation power density are significantly reduced. The HFBs induce continuous and lower heat load instead of high transient heat bursts on the divertor plate. The peak heat flux of the HFBs is about 10% of that caused by the unaffected ELMs. However, the ELM frequency decreases by about 50% for the pure Ne seeding discharge. Similar effect induced by pure Ar seeding was also observed on the HL-2A. Experimental observations suggest that the impurity mixture gas plays a role in changing the pedestal dynamics and there should be an optimal impurity ratio for efficient heat load control in ELMy H-mode plasmas [19].

3.3. ELM mitigation by RMP

Resonant magnetic perturbation (RMP) has been experimentally established as an efficient way of controlling ELMs in H-mode tokamak plasmas. ELM mitigation by RMP was achieved in HL-2A. We employ MARS-F code to carry out the RMP computation based on the HL-2A experimental configuration. It is found that the edge-peeling response is the main reason leading to the ELM mitigation as discussed below.

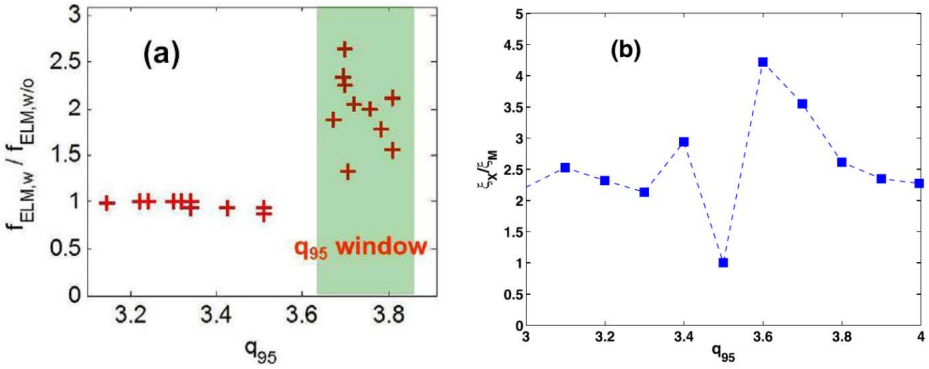

Figure 7: (a) The experimental ratio of the ELM frequency with RMP (shading region) to that without RMP; (b) the simulated ratio of the plasma surface displacement near the X-point to that near the outboard mid-plane. Reproduced with the permission from [20]

A direct comparison is carried out between experiments and modelling for HL-2A. Here, a database of the experimentally measured ELM frequency for a series of RMP discharges was created, where the edge safety factor q_{95} was varied. In the range of $q_{95} < 3.5$, no ELM mitigation was achieved in HL-2A (with odd parity coil configuration). However, clear ELM mitigation was achieved when $q_{95} > 3.6$ (Fig.7(a)), with more than doubling of the ELM frequency in certain cases. In the modelling, the ratio of the plasma surface displacement near the X-point ξ_X to that at the outboard mid-plane ξ_M is taken as an indicator of ELM mitigation. In other words, increase of ξ_X/ξ_M is equivalent to the increase of ELM frequency [21]. The MARS-F modeling [22, 23], based on the edge-peeling response model, predicts a mitigation

window (Fig.7(b)) which is slightly shifted towards the lower range of q_{95}. This may be partially due to the way the plasma equilibria are scanned in MARS-F, where only the total plasma current is varied, without modifying other equilibrium quantities such as the current profile and the plasma pressure. In experiments, these quantities may vary from shots to shots. Nevertheless, these MARS-F modeling results for HL-2A, though still not representing an exhausted study, already confirm the role of the edge-peeling response in the ELM mitigation that we have previously found in other devices [20].

4. TURBULENCE and TRANSPORT

Turbulence dynamics and the associated transports are an important topic as they play the important roles on realizing and maintaining high-confinement of the tokamak plasma. In last two years, significant progress was achieved on the HL-2A in understanding the modulation of turbulence by MHD, turbulent particle transport, turbulent stress and momentum transport, as well as formation of internal transport barrier in the situation with low central magnetic shear.

4.1. Modulation of turbulence by tearing mode in the core plasma

In recent years, the multi-scale interaction between large-scale modes and micro-scale turbulence has been found to play an important role in regulating turbulent transport [24] and eventually in the transition from low to high confinement mode. Apparently, detailed studies of interaction between macro-scale tearing modes and micro-scale turbulence are essential for further understanding the tearing instability and the island-induced transport, which will ultimately lead to developing a better control of tearing mode and optimization of plasma performance in fusion devices, such as ITER. Here, we report the experimental observation of modulation of both temperature and density fluctuations by a tearing mode (TM) island in the core of the HL-2A tokamak.

Plotted in Figs. 8(a)-(c) are the temporal evolution of the Electron Cyclotron Emission Imaging (ECEI) signal measured inside, near, and outside the $q = 1$ surface, respectively. It shows that when the X-point moves to the detection positions, the local T_e increases inside and nearby the $q = 1$ surface, the local T_e is roughly flatted across the O-point region, as shown in Fig. 8(b). As illustrated in [25], the flat T_e manifests the tearing mode feature, different from an ideal kink mode.

Figures 8(d) and (e) further display the time history of electron temperature fluctuations $\tilde{T}_e$ (integrated from 20-100 kHz) measured at R = 182.14 cm and Z = 3.46 cm and chord-averaged electron density fluctuations $\tilde{n}_e$ passing through the island region (integrated from 50-300 kHz), respectively. The envelopes of the temperature and density fluctuations are calculated via the Hilbert transform and depicted by the red curves. The fluctuation amplitudes in $\tilde{T}_e$ and $\tilde{n}_e$ are both modulated during the rotation of the m/n =1/1 island, i.e., minimum at the O-point and maximum at the X-point. The modulation on the envelops is approximately in phase with the interchange

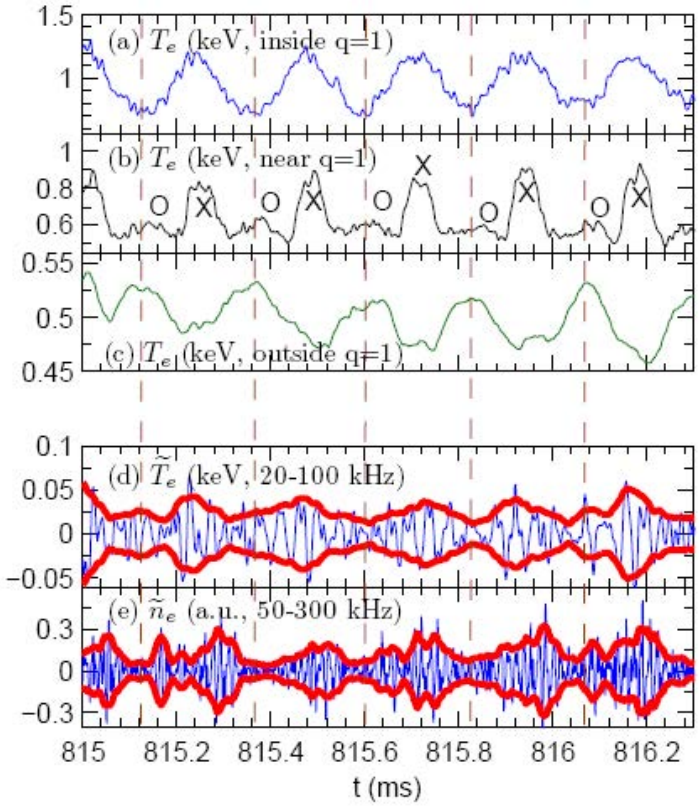

Figure 8: Temporal evolution of the ECEI signals measured (a) inside, (b) near, and (c) outside the q=1 surface. The vertical lines denote the O-point passing-by times. (d) and (e) show time trace of $\tilde{T}_e$ and $\tilde{n}_e$ respectively. The envelopes of fluctuations are depicted by the red curves in (d) and (e).

of the O- and X-point, consistent with gradient-driven turbulence since in the X/O-point region the local T_e or n_e gradient has the maximum/minimum value.

High spatiotemporal resolution two-dimensional (2D) images of $\tilde{T}_e$ show the first evidence that the turbulence modulation occurs only when the island width exceeds a certain threshold value ($w_c \approx 10\rho_i \approx 4$ cm) and the modulation is localized merely in the inner area of the island due to significant alteration of local profiles and turbulence drives. For large islands, turbulence radially spreading takes place across the island region. The results are generally consistent with theories and simulations [26].

4.2. Turbulence in the edge region

4.2.1. Turbulent stress at the plasma edge

Turbulence fluctuation strength, cross phase and coherence could impact the radial distribution of Reynolds stress as in the equation $\langle \tilde{v}_r \tilde{v}_\theta \rangle = \sigma_{\tilde{v}_r} \sigma_{\tilde{v}_\theta} \cdot \cos\langle \phi \rangle \cdot \langle \gamma \rangle$, and the cross phase $\cos\langle \phi \rangle$ between radial velocity perturbation $\tilde{v}_r$ and poloidal velocity perturbation $\tilde{v}_\theta$ plays an important role in the radial distribution of Reynolds stress.

This equation is perfectly verified in the HL-2A tokamak and recent results reveal that $E \times B$ shear would influence the coherence. In the region with a strong shear layer, measurements show that the cross phase is randomly scattered across the layer, which indicates a signature of incoherent phase slips and the radial distribution of the Reynolds stress is determined by the cross phase dynamics.In the weak shear region, the cross phase tends to stay in a coherent state (i.e., the phase locked state), where the turbulence fluctuation and coherence play a more important role [27].

Significant deviation from neoclassical prediction for mean poloidal flow in Ohmic and L mode discharges is deduced from direct measurements of the turbulent Reynolds stress [28]. The deviation increases with heating power. The turbulent poloidal viscosity is synthesized from fluctuation data, and is found to be comparable to the turbulent particle diffusivity. The intrinsic poloidal torque is deduced from synthesis, for the first time. PDFs of particle flux and Reynolds stress are obtained. Both exhibit fat tails and large kurtosis, suggest that the momentum transport process represented by the Reynolds stress is not well described by quasilinear calculations. It is implied that some potential new physical terms should be included in the present quasilinear model for describing turbulent momentum transport [29].

4.2.2. Coupling between density gradient and turbulent particle transport.

The experimental investigations of the dynamical coupling between density gradient and particle transport were performed in divertor configuration deuterium plasmas in the HL-2A tokamak under different confinement scenarios. Results show that the $E \times B$ turbulent flux behaves in such a way that the fluctuations are minimum in the proximity of the most probable density gradient, resulting in a non-monotonic relationship between particle transport and gradient.The size of transport events increases with gradient, which is consistent with the self-regulation of turbulent transport and gradients near marginal stability. The sign of particle flux is determined by the cross-phase between density and poloidal electric field fluctuations [30].

4.3. Formation of internal transport barrier (ITB) at low central magnetic shear

Formation of internal transport barrier (ITB) related to MHD activity was previously observed at DIII-D [31], ASDEX-U [32, 33], JET [34] and LHD [35]. In order to extrapolate these improved regimes to larger sized tokamaks and reactors, it is essential to determine the triggering conditions to form an ITB and to study the associated physics. This sub-section shows the progress of the understanding of the mechanism of ITB formation and the results about the kinetic electromagnetic instabilities in plasmas with ITB.

Recently, ITB at low central magnetic shear with $q_{min} \sim 1$ was observed during the nonlinear evolution of a saturated long-lived internal mode (LLM) in HL-2A discharges. As shown in Figure 9(c), an ITB is formed with a steep ion temperature profile, which is measured by charge exchange spectroscopy. Such steep ion temperature-gradient zone

locates around r/a=0.5-0.6 with $T_i > T_e$. The observed normalized ion temperature gradient (R/L_{T_i}) is about 10.6, which exceeds the value ($\sim$ 6.5) for a level without ITB. Here, R is the major radius and L_{T_i} is the scale length of T_i gradient defined as $L_{T_i} = aT_i/(T_i/d\rho)$, where a and $\rho = r/a$ are the minor radius and the normalized minor radius, respectively. In fig. 9(a), one can observe chirping modes at the time of the ITB formation. When the barrier forms, the turbulence is significantly reduced around ITB foot (r/a=0.6), as measured by reflectometry (fig. 9(b)). The simultaneous excitation of the ITB and the bursting internal mode occur only when q-profile remains flat in the core region. This implies the potential correlation between the internal instabilities and the ITB formation in reversed or weak shear plasmas. Further investigations in both theory and experiment are required to figure out the relationship between the internal instability and the ITB formation, in which the fast ion redistribution induced by instability may play a remarkable role [36].

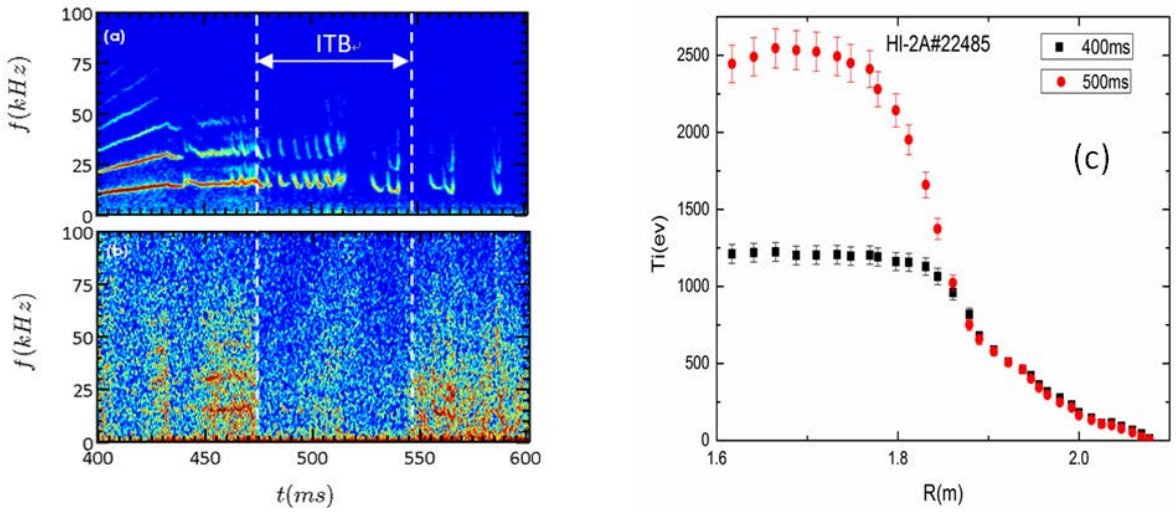

Figure 9: (a) Spectrogram of the central soft-X ray signal. (b) spectrogram of the density fluctuation at r/a=0.6 from reflectometry. (c) the ion temperature profiles during ITB formation of the $q = 1$ scenario.

4.4. High-frequency coherent modes in ITB plasma

In HL-2A ITB plasma with weak magnetic shear, kinetic electromagnetic instabilities (e.g., AITG/KBM) were confirmed and investigated. AITG/KBM stand for Alfvénic ion temperature gradient mode and kinetic ballooning mode, respectively. The experimental observations suggest that the stability of a high-frequency ($f = 80 - 200$ kHz) coherent modes (HFCMs) is relevant to the ITBs, and the strong T_i gradients potentially have important effects on the HFCMs. Theoretical analysis by the extended general fishbone-like dispersion relation (GFLDR-E) reveals that the mode frequencies scale with the ion diamagnetic drift frequency, and confirms that HFCM is a kind of kinetic electromagnetic instabilities (e.g. AITG). We provide clear experimental evidence of

the AITG modes and complex plasma behaviors which are fully consistent with the theoretical framework [37]. Furthermore, the observations reported in the previous work gave the first clear experimental identification of similar phenomena in some ohmic plasmas with high density and weak magnetic shear [38]. This experimental evidence paves the way to a more in-depth analysis of similar phenomena in fusion plasmas with non-perturbative energetic paricle populations, with the suggestive possibility of controlling plasma performance by a careful choice of plasma profiles in the weak shear core region typical of burning plasmas .

5. ENERGETIC PARTICLE PHYSICS

Studying the interaction of energetic particles (EPs) with collective modes is very important for burning plasmas, because these modes will degrade the confinement of the EPs(e.g. alpha particles being the plasma self-heating source in a fusion reactor). Moreover, these modes may play an important role in the thermal plasma confinement, and helium ash removal. Here, we focused on the mode observation/identification, phase space dynamics, nonlinear mode-mode coupling, and instability control [39] as well as multi-scale interaction among Alfvén mode and low frequency MHD mode.

5.1. New results related to ion fishbones on the HL-2A

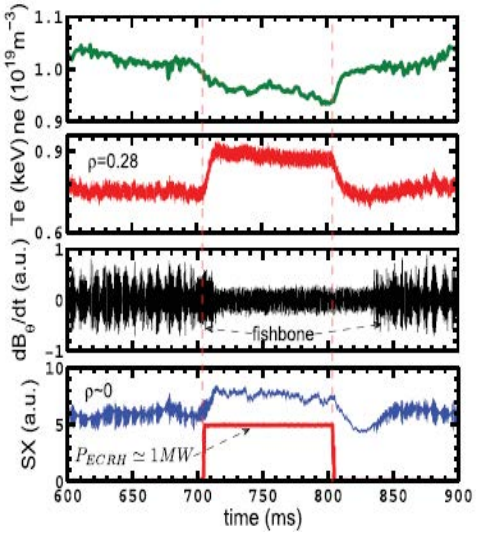

Figure 10: Typical discharge with $m/n = 1/1$ ion fishbone being stabilized by ECRH. Here, ρ is the normalized minor radius. Reproduced with the permission from [37]

5.1.1. Stabilization of m/n=1/1 fishbone by ECRH

The stabilization of $m/n = 1/1$ ion fishbone activities by Electron Cyclotron Resonance Heating (ECRH) were found on HL-2A [40]. Here, m and n are the poloidal

and toroidal mode numbers of an instability, respectively. The m/n=1/1 ion fishbone can be completely suppressed when the injected ECRH power exceeds a threshold (Fig.10). Figure 10 shows a typical experimental discharge. During NBI, the injected beam-ions stabilize the sawtooth and drive the fishbone instabilities. However after the high-power ECRH is switched on at t = 704 ms, the core electron temperature substantially increased, accompanied by a slight drop of density. More crucially, the fishbone was completely stabilized. When the ECRH was switched off at t = 804ms, the temperature and density began to change in the opposite direction, and the mode suppression lasted for another $t_d \sim 30$ms, which is close to the energy confinement time (τ_E). In fact, this experiment suggests that the high-power ECRH induces a sawtooth-free and fishbone-free operation regime during NBI. Theoretical analysis based on the fishbone dispersion relation, including the resistive effect, suggests that the magnetic Reynolds number plays a key role in the fishbone stabilization [37].

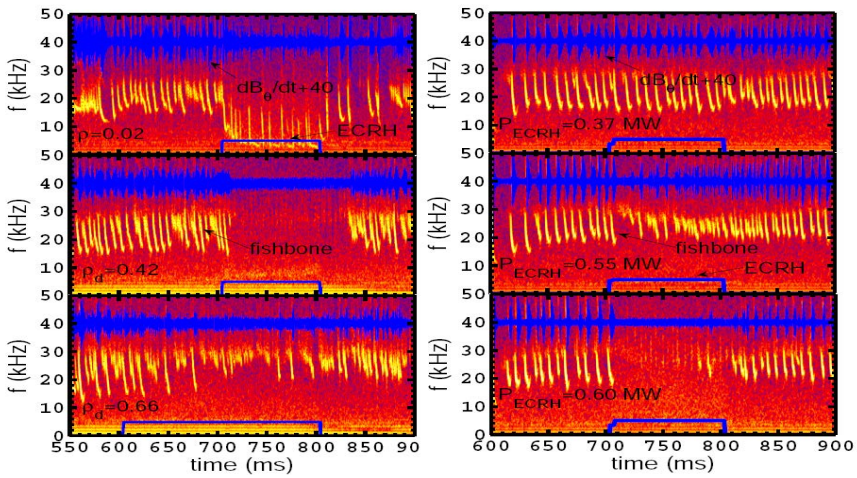

Figure 11: Effects of ECRH power and the deposition position on the stabilization of ion fishbone activities. Reproduced with the permission from figure 2 in [37]

By scanning the ECRH configuration parameters, we found that the fishbone stability depends not only on the injected power, but also on the radial deposition position of ECRH. The fishbone can be completely suppressed, when the injected ECRH power level exceeds a certain threshold. As shown in Fig. 11, at the same power level(i.e. $P_{ECRH} \simeq 1$MW),when the ECRH power is deposited on-axis ($\rho \sim 0$), the observed mode frequency obviously decreases, but the mode amplitude is only weakly reduced. When the power is deposited just outside of the q=1 rational surface ($\rho \sim 0.38$), the mode is fully stabilized. When the power is deposited off-axis ($\rho \sim 0.66$), the mode is partially stabilized. On the other hand, with the same deposition position ($\rho \sim 0.42$), ECRH at low power ($P_{ECRH} \simeq 0.37$MW) has hardly any stabilizing effect on the mode. Whilst with increasing the power level ($P_{ECRH} \simeq 0.55$MW) , the mode is progressively suppressed. The full stabilization was achieved at about $P_{ECRH} \simeq 0.6$MW. On DIII-D and LHD, it was demonstrated that ECRH was an effective way to suppress reversed

shear Alfvén eigenmode (RSAE) [41] and resistive interchange mode [42], respectively.

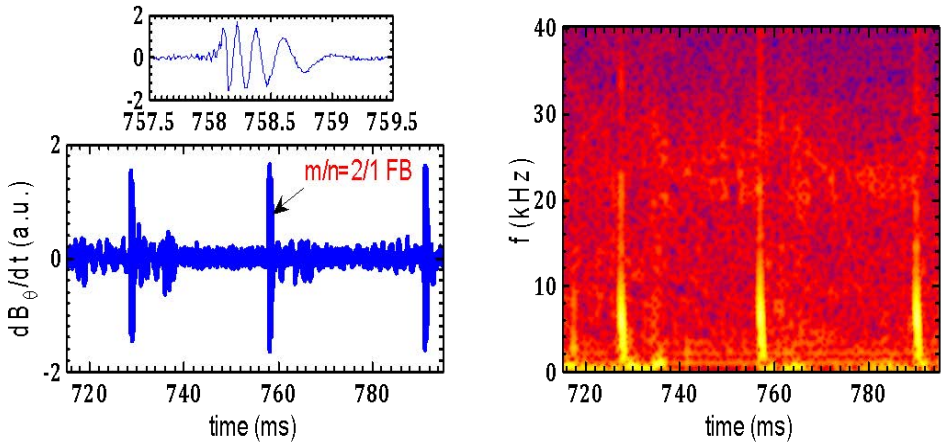

Figure 12: Typical $m/n = 2/1$ ion fishbone(FB) activities on the HL-2A.

5.1.2. Newly observed m/n=2/1 fishbone

The $m/n = 2/1$ ion fishbone activities were recently observed on the HL-2A(Fig.12). The appearance of $m/n = 2/1$ fishbone is perfectly reproducible. Figure 12 shows a typical shot. With the beam power $P_{NBI} \sim$ 1MW and relatively low density $n_e \sim 1.0 \times 10^{19}$ m^{-3}, the sawtooth is absent. However, during the auxiliary heating, the classical $m/n = 2/1$ TM is marginally unstable, with slowly rotating (f $<$ 2 kHz) and propagating in the electron diamagnetic drift direction. TM induces the large oscillation of electron temperature, but the Mirnov signal has the small amplitude ($|dB_\theta/dt| < 0.5$) due to the TM slow rotation. Specifically, it is found that an intense unstable bursting mode appears on the background with an marginally unstable TM. The mode-numbers of this new burst mode are $m/n = 2/1$. The mode frequency fast chirps downward within $\Delta t =$ 1ms. This mode propagates in the ion diamagnetic drift direction similar to the conventional $m/n = 1/1$ fishbone instability on HL-2A. This bursting phenomenon only occurs at the time when TM rotation direction changes from electron to ion diamagnetic drift. Otherwise, the $m/n = 2/1$ fishbone does not appear. All experimental results indicate that the TM resonantly interacts with energetic-ions. Similarly, a bursting fishbone-like mode in a spherical tokamak plasma with unstable neoclassical TM was observed on the TFTR device [43].

Nonlinear hybrid kinetic-MHD simulations using M3D-K reveal that the co-passing energetic-ions are responsible for the driving of the 2/1 fishbone, and the wave-particle resonance condition is satisfied at $\omega_\phi - 2\omega_\theta - \omega = 0$. Here, ω_ϕ, ω_θ and ω are the toroidal and poloidal projections of the transit frequency of passing particles, and the mode frequency, respectively [44].

5.2. Non-linear interaction between the AEs and TM

Multi-scale interactions among Alfven modes and low frequency MHD modes was observed on the HL-2A during the NBI injection, including nonlinear couplings between TAE/BAE and m/n = 2/1 TM near q = 2 surface, between AITG/KBM/BAE and m/n = 1/1 kink mode near q = 1 surface, and between m/n = 1/1 kink mode and high-frequency turbulence. Here, TAE and BAE stand for the toroidal Alfvén eigenmode and beta induced Alfvén eigenmode, respectively. Experimental results suggest that several couplings can exist simultaneously. Alfvénic fluctuations have an important contribution to the high-frequency turbulence spectra, and the couplings reveal the electromagnetic character of the turbulence. Multi-scale interactions via the nonlinear modulation process maybe enhance plasma transport and trigger sawtooth-crash onset[45].

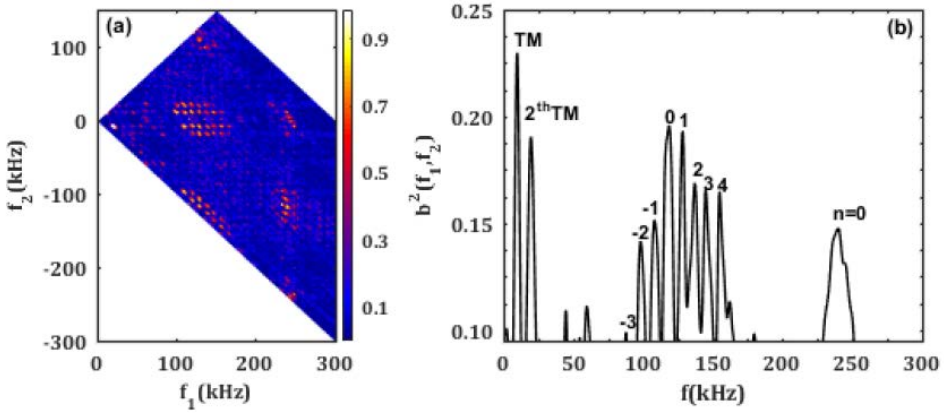

Figure 13: Nonlinear coupling phenomenon between TAEs and tearing mode. The squared bicoherence (a) and summed squared bicoherence (b) of the Mirnov signal

TAE driven by energetic-ion had been observed on HL-2A. The toroidal mode numbers for most unstable TAEs are $n = 1 \sim 3$. The TAEs were found to nonlinearly couple with TM and result in the appearances of series of Alfvénic modes (AMs). An axisymmetric mode within the ellipticity-induced frequency range, driven by TAEs coupling with TAEs, was found for the first time. The squared bi-coherence suggests that two AMs with the same absolute mode number, but with different propagating directions respect to the diamagnetic drift, couple together and lead to the generation of a high frequency mode with $n = 0$ (230-250kHz), shown as (Fig.13). The symmetrical mode with an 'anti-ballooning' feature was proved to be global Alfven eigenmodes (GAE) [46]. However, the mechanism of driving GAE here is different with the reported ones in [47] and [48]. . In addition, TAEs and BAEs driven by energetic-electrons were found and investigated in HL-2A ECRH or ECRH/LHCD plasmas [49].

5.3. Wave-particle non-linear interaction

Wave-particle non-linear interaction behaviors with chirping structures belongs to the chaotic regime were observed on the HL-2A. A Vlasov code, δf-COBBLES based on the

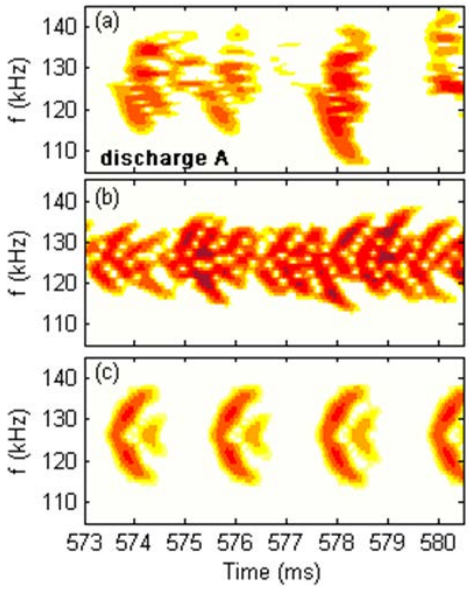

Figure 14: (a) The magnetic fluctuations spectrogram of discharge A (shot#26193). (b) Simulation obtained by Krook model. (c) Simulation based on Fokker-Plank model. Reproduced with the permission from [50].

so-called Berk–Breizman (BB) model, is applied to study the symmetric TAEs, with including Krook and Fokker-Plank collisional models. The analysis results suggest that the Fokker-Plank collision model yields better qualitative and quantitative agreement with the experimental observation (Fig.14).

Spectrum of TAEs with main-downward frequency chirping reproduced by Bump-On-Tail (BOT) code [51] with Fokker-Plank model shows a qualitative agreement with experimental observation. The interplay of diffusion and drag effect is essential to strengthen the clump movement, leading to fast ion distribution function clump-clump interactions. The main-downward chirping also shows that clump movement, which indicates that energy transfer from wave to particle is dominant. In many magnetic confinement devices, Alfvén modes were observed with stronger drive, which means that Alfvénic modes with main-downward chirping are relatively easy to be driven. It explains why main-downward chirping were observed more frequently [50].

6. SUMMARY

Since the 2016 Fusion Energy Conference, the HL-2A team has achieved significant progress in the areas of pedestal dynamics and L-H transition, ELM control, turbulence and transport and energetic particle physics as summarized below.

(i) The increase of the mean $\mathbf{E} \times \mathbf{B}$ shear flow plays a key role in triggering L-I and I-H transitions, which is mainly resulted from the ion pressure component. On the HL-2A, an inward particle flux induced by quasi-coherent mode (QCM) was found to be responsible for the increases of density and its gradient in the edge transport barrier

prior to each ELM.

(ii) ELMs are mitigated by LHCD, because of the regulation of turbulence intensity by the radial wavenumber spectral shift during LHCD. Both mitigation and suppression of ELMs was realized by LBO-seeded impurity. Furthermore, the 30% Ne mixture SMBI seeding robustly induces the ELM mitigation, and peak heat flux for the mitigation case is about 10% of that caused by the un-mitigated ELMs. The MARS-F modelling results for HL-2A confirm the role of the edge-peeling response in the ELM mitigation by RMP, which is consistent with the experimental observation.

(iii) The stabilization of m/n=1/1 ion fishbone activities by ECRH were found on the HL-2A. A new m/n=2/1 ion fishbone activities were observed recently, and the modelling indicates that passing fast ions dominantly contribute to the driving of 2/1 fishbone. The non-linear coupling between the Alfvén eigen-modes lead to the generation of a high frequency mode with n=0. Nonlinear wave-particle interaction behaviors with chirping structures belongs to the chaotic regime are observed on the HL-2A.

(iv) On the HL-2A tokamak, we found the modulation of electrostatic turbulence by rotating m/n=1/1 TM islands in the core plasmas. Highly resolved 2D ECEI measurements show the first evidence that the turbulence modulation occurs solely for large islands and the modulation takes place only in the inner half area of the island due to significant alteration of local profiles and turbulence drives between the X- and O-points.

In addition, several new diagnostics are recently updated and developed. A CO_2 dispersion interferometer [52] and a high sensitivity far-infrared laser interferometer [25] were developed for measuring the line-averaged density in time. The diagnostics for measuring density fluctuation were developed, including Phase Contrast Imaging (PCI) [53, 54, 55], Beam Emission Spectroscopy (BES) [56, 57] and He Gas-Puss-Imaging (He-GPI)[58]. Coherence Imaging Spectroscopy (CIS) was developed to monitor the 2D flow distribution. A new CO_2 laser collective Thomson scattering system was developed to measure high-k turbulence in the core plasma on the HL-2A. The analysis of some experimental data obtained by the above diagnostics is being carried out and, the associated physical results will be presented elsewhere in future.

The next experimental campaign of HL-2A will promote the following research aspects: the real time control of MHD instabilities(e.g. NTM, disruption), development of advanced ELM control techniques, physics of multi-scale interaction, as well as turbulence and transports.

Acknowledgments

The authors would like to thank all of the colleagues who have contributed to the HL-2A projects in the aspect of diagnostic developments and physics analysis. This work is supported by the Nuclear Power Development Research Project under grant No. H6600003-17, and National Key R&D Program of China under Grant Nos. 2015GB105000 and 2015GB104000. and the Chinese International Science and

Technology Cooperation Projects under grant no. 2015DFA61760.

References

[1] J. Cheng et al., EX/P5-6 presented at the 27th IAEA Fusion Energy Conference (Ahmedabad,India), 2018.
[2] A.Diallo et al., Nucl. Fusion **55** (2015) 053003.
[3] A.S. Liang et al., Phys. Plasmas **25** (2018) 022501.
[4] F. Ryter et al., Nucl. Fusion **57** (2016) 016004.
[5] Z. Yan et al., Phys. Rev. Lett. **112** (2014) 125002.
[6] E. Viezzer et al., Nucl. Fusion **54** (2013) 012003.
[7] G.L.Xiao et al., Phys. Plasmas **24** (2017) 122507.
[8] Y.Liang et al., Phys. Rev. Lett. **110** (2013) 235002.
[9] G.L. Xiao et al., EX/7-4 presented at the 27th IAEA Fusion Energy Conference (Ahmedabad,India), 2018.
[10] G.L.Xiao et al., submitted to Phys. Rev. Lett. (2018).
[11] G.L. Xiao et al., Phys. Plasmas **24** (2017) 122507.
[12] W.L. Zhong et al., Phys. Rev. Lett. **117** (2016) 045001.
[13] W.L. Zhong et al., Plasma Phys. Control. Fusion **59** (2017) 014030.
[14] Y.P. Zhang et al., Nucl. Fusion **58** (2018) 046018.
[15] P.W.Xi et al., Phys. Rev. Lett. **112** (2014) 085001.
[16] W.W. Xiao et al., Nucl. Fusion **54** (2014) 023003.
[17] H.Y.Lee et al., Phys. Plasmas **22** (2015) 122512.
[18] L.H. Yao et al., Nucl. Fusion **47** (2007) 1399.
[19] W.L.Zhong and et al., 23rd International Conference on Plasma Surface Interactions in Controlled Fusion Devices, Princeton University, NJ, USA, 17-22 June, 2018.
[20] Y.Q. Liu et al., Phys. Plasmas **24** (2017) 056111.
[21] Y.Q. Liu et al., Plasma Phys. Control. Fusion **58** (2016) 114005.
[22] Y.Q. Liu et al., Phys. Plasmas **17** (2010) 122502.
[23] Y.Q. Liu et al., Plasma Phys. Control. Fusion **58** (2016) 114005.
[24] L. Bardoczi et al., Phys. Rev. Lett. **116** (2016) 215001.
[25] Y.G. Li et al., Rev. Sci. Instrum. **88** (2017) 083508.
[26] M.Jiang et al., Nucl. Fusion (2019).
[27] D.Guo et al., Nucl. Fusion **58** (2017) 026015.
[28] T. Long et al., 2nd Asia-Pacific Conference on Plasma Physics, Kanazawa, Japan, 2018.
[29] R.Hong et al., Phys. Rev. Lett. **120** (2018) 205001.
[30] J.Q. Xu et al., Submitted to Nucl. Fusion (2018).
[31] K.L.Wong et al., Nucl. fusion **45** (2004) 30.
[32] S.Gunter et al., Nucl. fusion **41** (2001) 1283.
[33] R.C. Wolf et al., Plasma Phys. Control. Fusion **41** (1999) B93.
[34] E.Joffrin et al., Plasma Phys. Control. Fusion **44** (2002) 1203.
[35] K Toi et al., Nuclear Fusion **44** (2004) 217.
[36] Y.Liu et al., EX/P5-28 presented at the 27th IAEA Fusion Energy Conference (Ahmedabad,India), 2018.
[37] W. Chen et al., Nucl. Fusion **58** (2018) 056004.
[38] W. Chen et al., Europhys. Lett **116** (2016) 45003.
[39] V.Igochine et al., *Active control of magneto-hydrodynamic instabilities in hot plasmas*, Springer, 2015.
[40] W. Chen et al., Nucl. Fusion **58** (2018) 014001.
[41] V.Zeeland et al., Nucl. Fusion **49** (2009) 065003.
[42] X.D.Du et al., Phys. Rev. Lett. **118** (2017) 125001.

[43] E.D. Fredrickson, Phys. Plasmas **9** (2002) 548.
[44] W. Chen et al., EX/P5-20 presented at the 27th IAEA Fusion Energy Conference (Ahmedabad,India), 2018.
[45] W. Chen et al., Nucl. Fusion **57** (2017) 114003.
[46] P.W. Shi et al., Phys. Plasmasn **25** (2018) 062506.
[47] Z.Chang et al., Nucl. Fusion **35** (1995) 1469.
[48] K.G. McClements et al., Nucl. Fusion **42** (2002) 1155.
[49] L.M. Yu et al., Phys. Plasmas **25** (2018) 012112.
[50] Y.M. Hou et al., Nucl. Fusion **58** (2018) 096028.
[51] M.K. Lilley et al., Phys. Plasmas **17** (2010) 092305.
[52] H.X. Wang et al., Rev. Sci. Instrum. **88** (2017) 103502.
[53] S.B.Gong et al., Fusion Eng. Des. **123** (2017) 802.
[54] S.B.Gong et al., J. Instrumentation **12** (2017) C10005.
[55] S.B.Gong et al., Fusion Eng. Des. **133** (2018) 99.
[56] R. Ke et al., Rev. Sci. Instrum. Accepted (2018).
[57] R. Ke et al., JINST **13** (2018) P05027.
[58] B. Yuan et al., JINST **13** (2018) C03033.